FINAL TECHNICAL REPORT – August 29, 2012

I. GRANT INFORMATION

Grant Number	HR0011-08-1-0084
Title of Research	Nanostructured Composite Materials for High Temperature Thermoelectric Energy Conversion
Principal Investigator	Dr. Charles J. O'Connor
Organization	University of New Orleans, New Orleans, LA 70148

II. SUMMARY

The goals of this project were to synthesize, characterize and model bulk nanostructured composite materials for thermoelectric energy conversion applications. The objective was to produce materials which demonstrate an increase in intrinsic thermoelectric efficiency of a factor of two or more over existing commercially-available materials.

The research project consists of

- The synthesis of two main classes of materials, half-Heusler intermetallic bulk nanocomposites and bismuth-telluride based nanocomposites;
- Complete structural and mechanical characterization of the materials;
- Thermal and electrical transport characterization the materials;
- Simulation of electronic band structure and electronic transport; and
- Modeling and prediction of device and system performance.

The project involved eight faculty investigators from AMRI, Chemistry, Physics and Mechanical Engineering at UNO and one faculty investigator at Michigan State University. These investigators are listed below.

INVESTIGATOR	DEPARTMENT	RESEARCH AREA
P. F. P. Poudeu	Chemistry/AMRI	Nanostructure half-Heusler materials, high-temperature transport measurements
K. Stokes	Physics/AMRI	Bismuth telluride/metallic nanoparticle composites, transport measurements
J. Wiley	Chemistry/AMRI	Chemical synthesis of nanoparticles compounds
C.J. O'Connor	Chemistry/AMRI	Chemical synthesis of nanoparticle compounds
P. Schilling	Mech. Eng./AMRI	Mechanical alloying of half-Heusler compounds, mechanical properties measurements
P. Herrington	Mech. Eng.	Finite element modeling of devices
M. Verges	Mech. Eng.	Mechanical properties of nanocomposites measurement and analysis
D. Hui	Mech. Eng.	Novel nanocomposite synthesis
S.D. Mahanti	Physics, Michigan State Univ.	Band structure and transport properties simulations.

III. RESEARCH HIGHLIGHTS

Thermoelectric performance of bulk $Zr_{0.5}Hf_{0.5}Co_{1-x}Rh_xSb_{0.99}Sn_{0.01}$ half-Heusler alloys. As in the Ir-substituted system, substitution of Rh for Co causes the material to change from n-type to p-p-ptype. The pure Co alloy as a small negative Seebeck coefficient; increasing the Rh concentration results in a relatively large positive Seebeck coefficient. For Rh, the highest Seebeck coefficient is approximately 125 μV/K at 700 K for x=0.6 Rh. Higher Rh concentrations result in lower Seebeck coefficient. However, for Rh concentrations >0.9, the electrical conductivity displays an activated behavior, increasing with increasing temperature.

The effect of impurity doping in HfCoSb half-Heusler system. Band structure and transport property calculations were performed on HfCoSb as a function of carrier (hole) concentration and impurity species ($HfCoSb_{0.75}X_{0.25}$, X=Ge, Sn, Pb). Transport property calculations for HfCoSb showed the highest power factor near a hole concentration of $4x10^{21}/cm^3$ corresponding to doping of 25%. Doping atom had little effect on the electronic transport.

Nickel oxide nanoparticles prepared by combustion synthesis. We developed a combustion technique for the synthesis of nickel oxide (NiO) nanoparticles. Up to 2.0 g of nanoparticle can be produced with particle sizes from 3 to 350 nm depending on the reaction conditions and post-synthesis annealing. These nanoparticles are used as nanometer-scale inclusions for the creation of half-Heusler-based nanocomposites.

Synthesis and characterization of HfO_2 Nanoparticles for nanoinclusion in half-Heusler matrix. Hafnium oxide (HfO_2) nanoparticles have also been produced as inclusions for nanocomposites. Here, the nanoparticles are synthesized by sol-gel chemistry using hafnium(IV) tert-butoxide and ammonium hydroxide. Annealing at 500ºC results in highly crystalline HfO_2. Although the particles have irregular morphology, they are suitable as nanoinclusions in our composites.

Synthesis of ZrNiSn by mechanical alloying. Mechanical alloying (or ball-milling) is being explored as an alternate synthesis method for half-Heusler alloys. This technique, in which elemental constituents are placed in a high-energy ball mill in an inert atmosphere, eliminates the high temperature processing (melting, arc melting). After 10 hr, phase pure ZrNiSn is produced with a grain size of approximately 11 nm. The powders were consolidated by both conventional hot pressing and spark plasma sintering. A detailed analysis of the x-ray diffraction pattern yields grain size and strain as a function ball-mill reaction time and method of consolidation.

Measurement of modulus and hardness of nanocomposites. We have measured the modulus and hardness of Ir- and Rh-substituted half-Heusler compounds consolidated hot pressing and spark-plasma sintering. The measurements were made with Agilent G200 Nano Indenter acquired as part of this grant. This system is capable of Continuous Stiffness Measurements (CSM) with allows the determination of mechanical properties as a function of penetration

depth of the nanoprobe. The system also has a nanopositioning stage for positioning and scanning. We find that the elastic stiffness is high when compared to other materials being considered for thermoelectric applications. The presence of Ir or Rh did not have a significant effect on the stiffness or hardness of this half-Heusler compound.

Finite element analysis modeling of thermoelectric devices. FEA modeling was performed on device geometries to obtain the temperature distribution of thermoelectric generator (TEG) device. This allowed us to numerically predict device performance, determine thermal/mechanical stresses, estimate allowable stress/strain limits of the material and optimize device geometry. The FEA simulations are performed with ANSYS. Required inputs for each material (n-type and p-type compounds) are thermal conductivity, specific heat, electrical conductivity, Seebeck coefficient, Young's modulus and Poisson's ratio. All these parameters are routinely measured by the research team. We have verified the model for a single couple and a more realistic device consisting of 17 couples (34 materials), copper tabs, ceramic substrates and a matched load external resistor.

Investigation of microstructure, thermoelectric; and mechanical properties of bulk p-type half Heusler materials. Improvement of the thermoelectric figure of merit can be achieved in p-type $Zr_{0.5}Hf_{0.5}Co_{1-x}Rh_xSb_{1-y}Sn_y$ and $Zr_{0.5}Hf_{0.5}Co_{1-x}Ir_xSb_{1-y}Sn_y$ systems via thermal conductivity reduction through mass fluctuation phonon scattering and enhancement in power factor through doping. Maximum *ZT* at 800 K are 0.13 for $Zr_{0.5}Hf_{0.5}Co_{0.3}Ir_{0.7}Sb_{0.9}Sn_{0.1}$ and 0.2 for $Zr_{0.5}Hf_{0.5}Co_{0.4}Rh_{0.6}Sb_{0.8}Sn_{0.2}$.

Investigation of microstructure, thermoelectric; and mechanical properties of bulk n-type $Zr_{0.5}Hf_{0.5}Ni_{1-x}Pd_xSn_{0.99}Sb_{0.01}$ materials. Single phase half Heusler alloy of composition $Zr_{0.5}Hf_{0.5}Ni_{1-x}P_xSn_{0.99}Sb_{0.01}$ with x=0 to 1.0 were synthesized by high-temperature solid-state diffusion. The influence of substitution of Pd at Ni site on the high temperature thermoelectric properties has been studied. The addition of Pd was found to increase the resistivity and decrease thermal conductivity.

Investigation of thermoelectric properties of half Heusler nanocomposites $Zr_{0.5}Hf_{0.5}Ni_{0.8}Pd_{0.2}Sn_{0.99}Sb_{0.01}$ composites with x wt% (WO_3, HfO_2, NiO, or PdGe eutectic) have been studied. Generally, the inclusion of these nanoparticles serves to increase electrical conductivities but decrease the magnitude of the Seebeck coefficient with respect to their host matrixes, consistent with a semiconductor/metal composite material.

IV. TECHNICAL ACCOMPLISHMENTS

A. Half Heusler Compounds

We have successfully synthesized half-Heusler alloys with general compositions $[Zr_{0.5}Hf_{0.5}][Ni_{1-y}Pd_y][Sn_{0.99}Sb_{0.01}]$; $[Zr_{0.5}Hf_{0.5}][Co_{1-y}Rh_y][Sb_{0.99}Sn_{0.01}]$ and $[Zr_{0.5}Hf_{0.5}][Co_{1-y}Ir_y][Sb_{0.99}Sn_{0.01}]$. A full suite of thermoelectric measurements including electrical conductivity, thermopower as well as thermal conductivity were performed on hot-pressed materials. We have also fabricated

$[Zr_{0.5}Hf_{0.5}][Ni_{1-y}Pd_y][Sn_{0.99}Sb_{0.01}]$ nanocomposite using NiO nanoparticles as inclusion phases and created uniform HfO_2 nanoparticles for use in the fabrication of half-Heusler nanocomposites. In addition, we were able to determine suitable conditions for *in situ* grow of PdGe nanoparticles within half-Heusler alloy with composition $[Zr_{0.5}Hf_{0.5}][Ni_{1-y}Pd_y][Sn_{0.99}Sb_{0.01}]$.

1. Thermoelectric properties of Bulk $Zr_{0.5}Hf_{0.5}Co_{1-x}Ir_xSb_{0.99}Sn_{0.01}$ Half-Heusler Alloys

Several samples with general composition $Zr_{0.5}Hf_{0.5}Co_{1-x}Ir_xSb_{0.99}Sn_{0.01}$ (x = 0.0, 0.1, 0.3, 0.5, 0.7) were synthesized by high temperature solid-state reaction and the thermoelectric properties of the hot-pressed pellets were measured in the temperature range from 300K to 800K. Well mixed high purity powders of the elements, weighed in the appropriate stoichiometry, were vacuum-sealed in silica tubes and annealed at 900 °C for several days. The effect of the variation of Ir concentration on the thermoelectric properties of the samples was investigated. At 300 K the thermal conductivity of $Zr_{0.5}Hf_{0.5}Co_{1-x}Ir_xSb_{0.99}Sn_{0.01}$ decreases with increasing Ir content from ~6.5 W/m·K for x = 0, reaches a minimum of ~4.0 W/m·K for x = 0.3 and increases thereafter with further addition of Ir. The thermal conductivity of $Zr_{0.5}Hf_{0.5}Co_{1-x}Ir_xSb_{0.99}Sn_{0.01}$ decreases with rising temperature and the smallest value of ~2.5 W/m·K was observed at 700K for x = 0.3. All samples show p-type semiconducting behavior in the measured temperature range. At 300 K, the electrical conductivity and thermopower of $Zr_{0.5}Hf_{0.5}Co_{1-x}Ir_xSb_{0.99}Sn_{0.01}$ materials increase with increasing Ir concentration. The largest electrical conductivity and thermopower values of 140 μW/K and 150 S/cm was observed at 300 K for x = 0.7.

Figure 1a shows the X-ray powder diffraction of the synthesized $Zr_{0.5}Hf_{0.5}Co_{1-x}Ir_xSb_{0.99}Sn_{0.01}$ samples. All patterns could be indexed with the cubic ZrNiSn structure-type (F-43m) and include additional small peaks of ZrO_2 or HfO_2 impurity phases. The refined lattice parameters (Figure 1B) increase linearly with increasing Ir content. In addition, the densities of the synthesized powder samples also increase linearly with increasing Ir concentration (Figure 1b). The

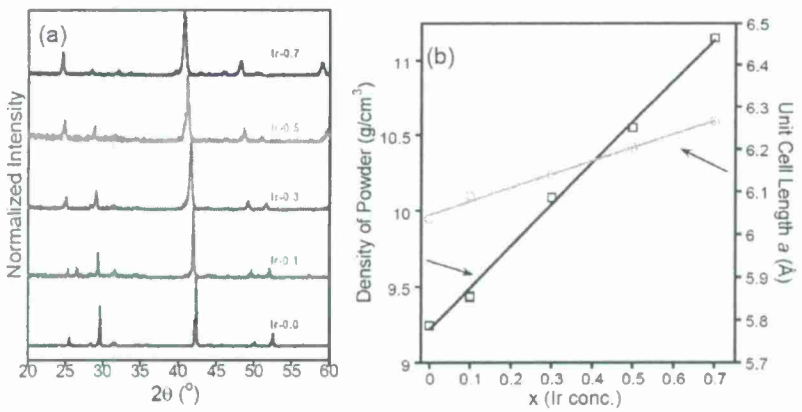

Figure 1. (a) PXRD of hot pressed pellets of Zr0.5Hf0.5Co1-xIrxSb0.99Sn0.01 samples. (b) Unit cell parameters and densities of Zr0.5Hf0.5Co1-xIrxSb0.99Sn0.01 samples plotted as a function of Ir concentration.

observed trend follows Vegard's Law and indicates that "true" solid solutions are obtained when Co is increasingly substituted by Ir in the $Zr_{0.5}Hf_{0.5}Co_{1-x}Ir_xSb_{0.99}Sn_{0.01}$ materials. The formation of the "true" solid solution is important for the reduction of the lattice thermal conductivity of $Zr_{0.5}Hf_{0.5}Co_{1-x}Ir_xSb_{0.99}Sn_{0.01}$ materials through mass fluctuation phonon scattering.

Table I shows the percent densification of the hot pressed pellets of the synthesized materials. The percent densification was obtained by dividing the pellet density (calculated from sample geometry and mass) by the "true" density of the powder sample measured using He gas pycnometry. All pellets used for the properties measurements showed at least 97% densification.

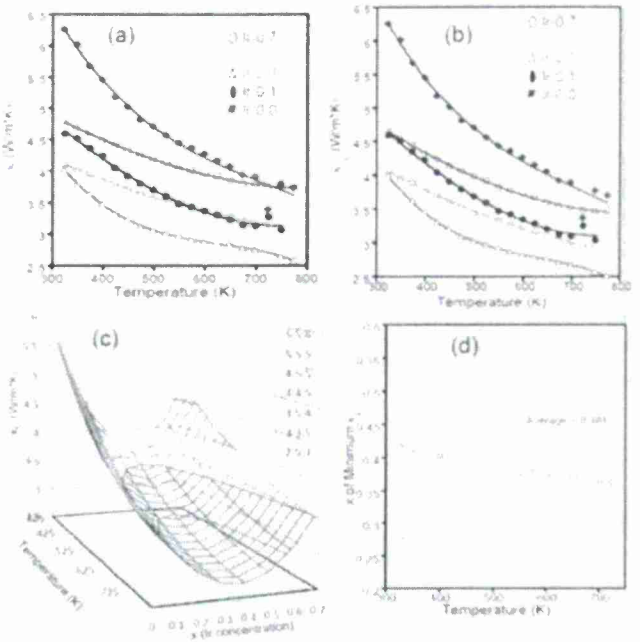

Figure 2. Thermal conductivities of $Zr_{0.5}Hf_{0.5}Co_{1-x}Ir_xSb_{0.99}Sn_{0.01}$ samples plotted as a function of temperature (a) total; (b) lattice contribution. (c) Variation of lattice thermal conductivity with Ir concentration, x, at various temperatures. (d) Variation of Ir concentration of minimum lattice thermal conductivity for $Zr_{0.5}Hf_{0.5}Co_{1-x}Ir_xSb_{0.99}Sn_{0.01}$ samples plotted as a function of temperature

Table I: Density and Compaction of $Zr_{0.5}Hf_{0.5}Co_{1-x}Ir_xSb_{0.99}Sn_{0.01}$ half-Heusler samples

Sample Code	Pycnometric Density of powder (g/cm^3)	Geometrical Density of Pellet (g/cm^3)	% Densification
Ir-0.0	9.245(7)	8.993	97.3%
Ir-0.1	9.438(7)	9.162	97.1%
Ir-0.3	10.085(14)	9.840	97.6%
Ir-0.5	10.547(16)	10.230	97.0%
Ir-0.7	11.152(12)	10.877	97.5%

The total thermal conductivity of the synthesized bulk $Zr_{0.5}Hf_{0.5}Co_{1-x}Ir_xSb_{0.99}Sn_{0.01}$ half-Heusler samples are shown in Figure 2A. Regardless of the Ir content, the total thermal conductivities of the materials decrease monotonically with increasing temperature. For example, the thermal conductivity of $Zr_{0.5}Hf_{0.5}Co_{0.7}Ir_{0.3}Sb_{0.99}Sn_{0.01}$ (x = 0.3) decreases from ~4 W/m·K at 300 K to ~2.5 W/m·K at 750K. The lattice component of the thermal conductivity calculated using the equation $\kappa_{total} = \kappa_{e^-} + \kappa_L$, (where κ_{total} is the total thermal conductivity, $\kappa_{e^-} = 2.44 \times 10^{-8}\sigma T$, is the electrical component of the thermal conductivity and κ_L is the lattice component of the thermal conductivity) was found to follow a similar trend (Figure 2B). The smallest lattice thermal conductivity, ~2.6 W/ m·K was observed at 750 K for sample with x = 0.3. Regardless of the

temperature, the lattice thermal conductivity of the materials decreases with increasing Ir concentration, goes through a minimum and then increases with further increases in Ir content (Figure 2C). The change in lattice thermal conductivity as a function of x (Ir content) at a given temperature was approximated by a second-order polynomial. The quality of the fit of this function was found to produce $R^2 > 0.9$ for all temperatures. The minima of the polynomial function was used to determine the approximate Ir concentration of minimum lattice thermal conductivity (Figure 2D). The value of x giving the minimum lattice thermal conductivity appears to decrease with increasing temperature. However, the observed variation of the $x_{(minimal)}$ as a function of temperature is very small. The average value $x_{(minimal)} = 0.38$ was determined as the optimum Ir concentration necessary to reduce the thermal conductivity of $Zr_{0.5}Hf_{0.5}Co_{1-x}Ir_xSb_{0.99}Sn_{0.01}$ materials to the minimum obtainable for this solid solution. The optimal value of x will be used in future experiments aimed at optimizing the thermoelectric performance of half-Heusler phases with general composition $Zr_{1-y}Hf_yCo_{1-x}Ir_xSb_{1-z}Sn_z$.

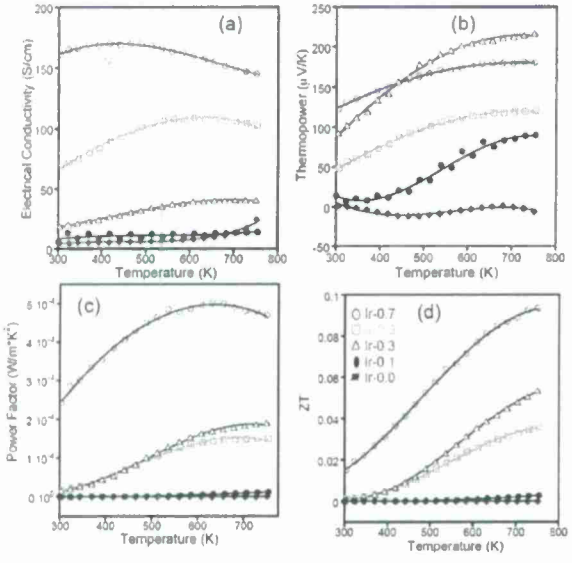

Figure 3. Temperature dependence of charge transport properties of $Zr_{0.5}Hf_{0.5}Co_{1-x}Ir_xSb_{0.99}Sn_{0.01}$ samples. (a) Electrical conductivity; (b) Thermopower; (c) Power factor. (d) Figure of merit, ZT, of $Zr_{0.5}Hf_{0.5}Co_{1-x}Ir_xSb_{0.99}Sn_{0.01}$ samples.

Figure 3A shows the electrical conductivity of the $Zr_{0.5}Hf_{0.5}Co_{1-x}Ir_xSb_{0.99}Sn_{0.01}$ samples. The electrical conductivity increases with increasing Ir concentration. For compositions with x = 0 and 0.1, the electrical conductivity is very small (~ 2 S/cm at 300K) and increases slowly with rising temperature. When the Ir content is increased to x = 0.3, the electrical conductivity of the material at 300K jumps from 2 S/cm to approximately 15 S/cm. As the temperature increases, the electrical conductivity of this particular composition also increases indicating that the material is an intrinsic semiconductor. At Ir concentration x = 0.5, the room temperature value of the electrical conductivity is ~ 60 S/cm. The electrical conductivity increases further to 155 S/cm at 300 K when the Ir content is increased to x = 0.7. The electrical conductivity versus temperature curves for the last two compositions showed a maximum of conductivity at 600K (x = 0.50 and 450 K (x = 0.7). This trend suggests that, the conduction type within the $Zr_{0.5}Hf_{0.5}Co_{1-x}Ir_xSb_{0.99}Sn_{0.01}$ varies with increasing Ir content. At low Ir content (x = 0, 0.1 and 0.3), the samples behave as normal semiconductor. As the Ir content increases, the $Zr_{0.5}Hf_{0.5}Co_{1-x}Ir_xSb_{0.99}Sn_{0.01}$ materials increasing evolve towards degenerate semiconducting behavior.

The temperature dependence of the thermopower of $Zr_{0.5}Hf_{0.5}Co_{1-x}Ir_xSb_{0.99}Sn_{0.01}$ samples are shown in Figure 3B. All samples are p-type semiconductors at room temperature, as indicated by the positive values of the thermopower. Samples with low Ir concentration (x = 0, 0.1) show very small thermopower values at 300K. For composition with x = 0, the thermopower is almost

zero at 300 K and became negative as the temperature increases. For composition with x = 0.1, a thermopower of 10 μV/K was measured at 300K.The thermopower of this sample increases to ~60 μV/K at 750 K. Larger thermopowers were measured for samples with higher Ir content (x = 0.3, 0.5 and 0.7). For composition with x = 0.3, a thermopower value of ~50 μV/K was measured at 300 K. The room temperature values of the thermopower increase to 100 μV/K for x = 0.5 and ~140 μV/K for x = 0.7. The thermopowers of all three compositions increase monotonically with increasing temperature. The composition with x = 0.3 showed the strongest temperature dependence, and a maximum thermopower value of ~ 220 μV/K was observed at 750 K. The power factors of all five compositions are shown in Figure 3C. Compositions with x = 0, 0.1, 0.3 and 0.5 showed a low power factor due to the low values of the electrical conductivities and/or the thermopower. The highest power factor of ~5μW/cm·K^2 was obtained at 750K for the sample with x = 0.7. The thermoelectric figures of merit of the $Zr_{0.5}Hf_{0.5}Co_{1-x}Ir_xSb_{0.99}Sn_{0.01}$ samples are shown in Figure 3D. In general, $Zr_{0.5}Hf_{0.5}Co_{1-x}Ir_xSb_{0.99}Sn_{0.01}$ samples show very poor figures of merit at 300K. For composition with x = 0.3, 0.5 and 0.7, the ZT values rapidly increase with increasing temperature. A maximum ZT of ~0.1 was obtained at 750 K for composition with x = 0.7.

2. *Thermoelectric properties of $Zr_{0.5}Hf_{0.5}Ni_{1-x}Pd_x Sn_{0.99}Sb_{0.01}$ alloys ($0.0 \leq x \leq 1.0$)*

Thermal and electrical transport measurements were made in the temperature range from 300 K (20°C) to 750 K (475°C). Figure 4 shows the results of the electrical conductivity and Seebeck coefficient measurements. The conductivity varies from 1000 to 3000 S/cm with the highest conductivity for the x=0.6 compound (this compound also has the lowest Seebeck coefficient). All samples are n-type semiconductors with the Seebeck coefficient varying between -50 μV/K to -170 μV/K at high temperature. The largest Seebeck coefficient in found in the x=0.2 compound.

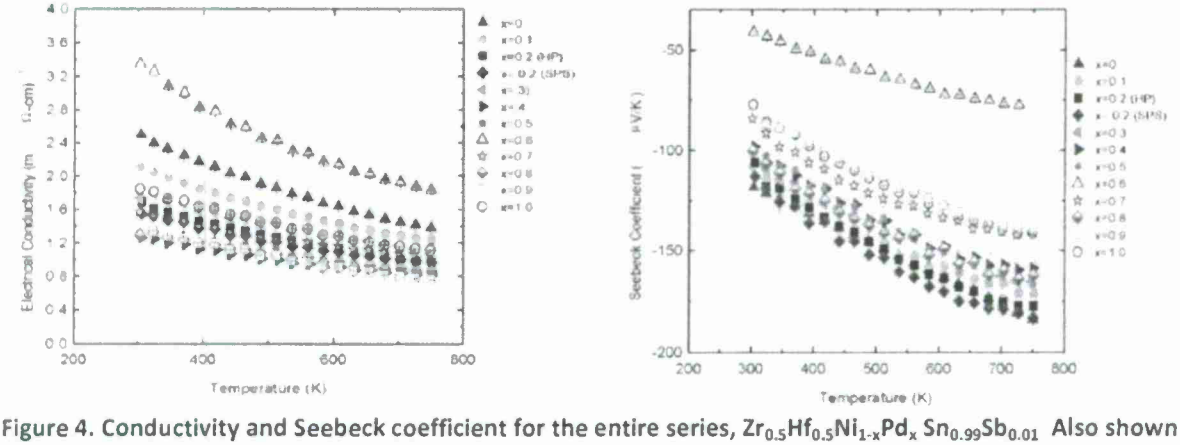

Figure 4. Conductivity and Seebeck coefficient for the entire series, $Zr_{0.5}Hf_{0.5}Ni_{1-x}Pd_x Sn_{0.99}Sb_{0.01}$ Also shown is the comparison between the hot pressed samples (labeled HP) and spark-plasma sintered samples (labeled SPS).

Power factor ($S^2\sigma$) is shown in Figure 5 along with the thermal conductivity. The largest power factor is found in the x=0 (pure Ni) compound. The power factor seems to decrease with increasing Pd concentration (increasing x), except for x=0.6, which has the lowest power factor. Thermal conductivity is shown in Figure 5 (right). The lowest thermal conductivities are around 4 W/m-K for the x=0.4, 0.5 and 0.8 samples.

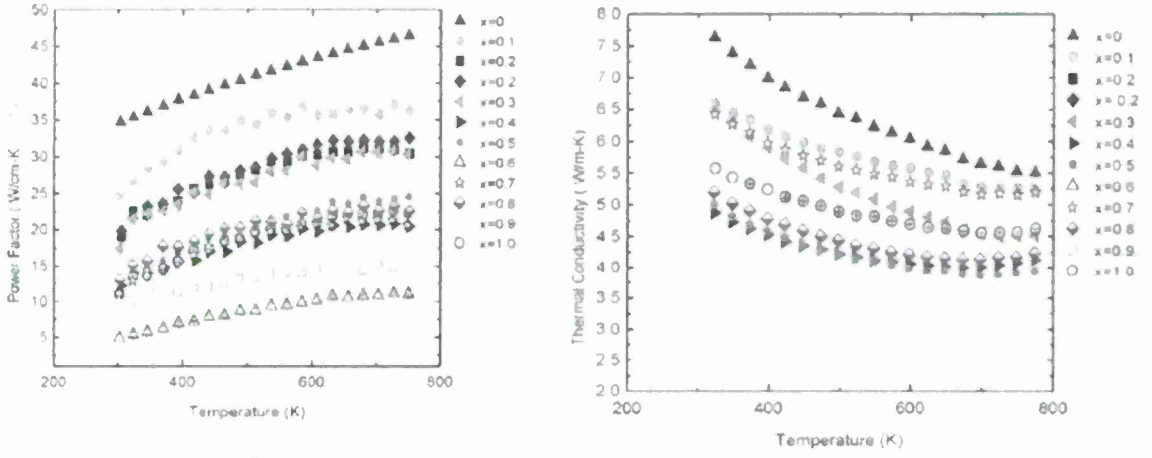

Figure 5. Power factor ($S^2\sigma$) and thermal conductivity for the half-Heusler series.

Finally, figure of merit, (*ZT*) is shown in Figure 6. Despite having the highest thermal conductivity, the highest figure of merit is *ZT*=0.63 and is found in the pure Ni sample (x=0).

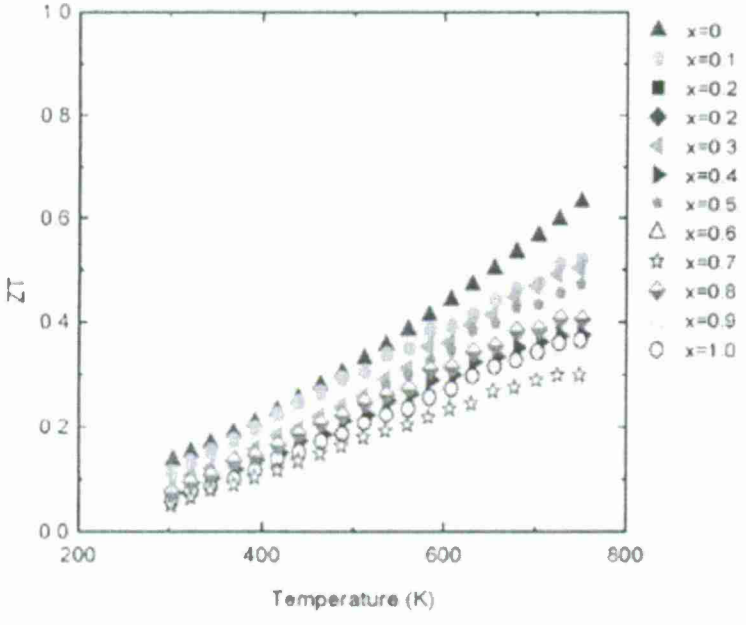

Figure 6. Figure of merit, ZT, for the for the half-Heusler series.

Our investigation on the effects of Ir substitution on the thermoelectric performance of $Zr_{0.5}Hf_{0.5}Co_{1-x}Ir_xSb_{0.99}Sn_{0.01}$ half-Heusler alloys showed a complete solubility of Ir on the Co site for $0 \le x \le 0.7$. The lattice thermal conductivities of hot pressed pellets of the synthesized materials decrease with increasing Ir content to an optimum concentration of $x \sim 0.38$. For composition with x = 0.3, the lowest lattice thermal conductivity of ~2.5 W/m·K was obtained at 750K. This optimum Ir concentration (x = 0.38) will be used in future studies aiming at optimizing the thermoelectric performance of the $Zr_{1-y}Hf_yCo_{1-x}Ir_xSb_{1-z}Sn_z$ half-Heusler materials. From the $Zr_{0.5}Hf_{0.5}Ni_{1-x}Pd_x\ Sn_{0.99}Sb_{0.01}$ study, we found that the most promising materials for the thermoelectric generator applications are the compounds with x=0, x=0.5 and x=0.8.

B. Band Structure Calculations

We have studied the electronic structure and electronic transport properties of simple half-Heusler (HH) compounds (*AB*Sb, *A*=Hf,Zr; *B*=Ir,Co) to understand the interplay between the band structure and the thermoelectric behavior such as thermopower, electrical conductivity, and hence power factors. The calculations are performed by the projector augmented wave (PAW) method as implemented in VASP with Perdew-Burke-Ernzerhof (PBE) generalized gradient approximation (GGA) for the exchange-correlation potential. A plane-wave cutoff energy of 400 eV and an energy convergence criterion of 10^{-4} eV for self-consistency are adopted. For transport property calculations, we have used a 41×41×41 Monkhorst-Pack k-point sampling for the primitive unit cell with three atoms. For cases of impurity study, we have used a cubic cell with twelve atoms. From obtained band structure, we have calculated the transport properties such as thermopower, electrical conductivity, hence power factor, and electronic thermal conductivity using Boltzmann transport equations.
Some of our results are summarized below.

1. *Electronic Structure and thermoelectric properties of Sb-based half-Heusler compounds*

We have studied the electronic band structure and thermoelectric properties of *AB*Sb (*A*=Hf,Zr; *B*=Ir,Co) half-Heusler compounds (Figure 7). The valence band maximum occurs at the L point in the Cocompounds while it is at the Γ point in the Ir-compounds. The position and hybridization of a *s*-like conduction band vis-à-vis the hybridized *d*-bands of Co(Ir) determines the nature of the conductions bands near the band gap region. In addition, there is a direct band gap at the Γ point in HfIrSb, whereas in the other three compounds, the band gap is indirect, either between Γ and X or between L and X points. As shown in Fig. 8, the Co compounds usually give large thermopowers, both for *p*-and *n*-dopings. However ZrIrSb, due to its interesting conduction band structure, gives the best *n*-type thermopower at higher temperatures.

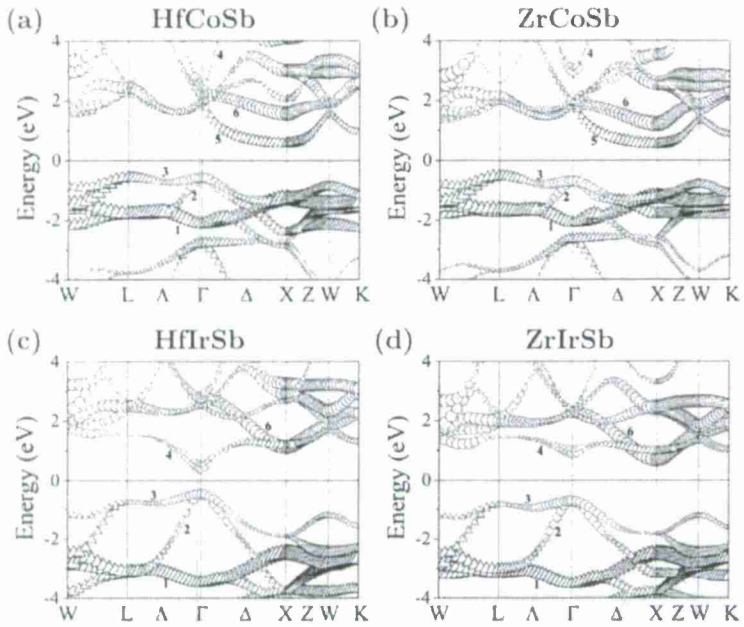

Figure 7. The contribution of each atoms in the band structure of (Hf,Zr)(Co,Ir)Sb compounds : circles (○) for *d*-orbital of Hf/Zr, triangles (Δ) for *d*-orbital of Co/Ir, stars (☆) for *p*-orbital of Sb, and diamonds (◇) for *s*-orbital of Sb. The size of the symbols represents the strength of the contribution. The Fermi level is set to be zero energy. The band structure near the Fermi energy for (a) HfCoSb, (b) ZrCoSb, (c) HfIrSb, and (d) ZrIrSb along W-L-Γ-X-Z-W-K. The Fermi level is set to be zero energy.

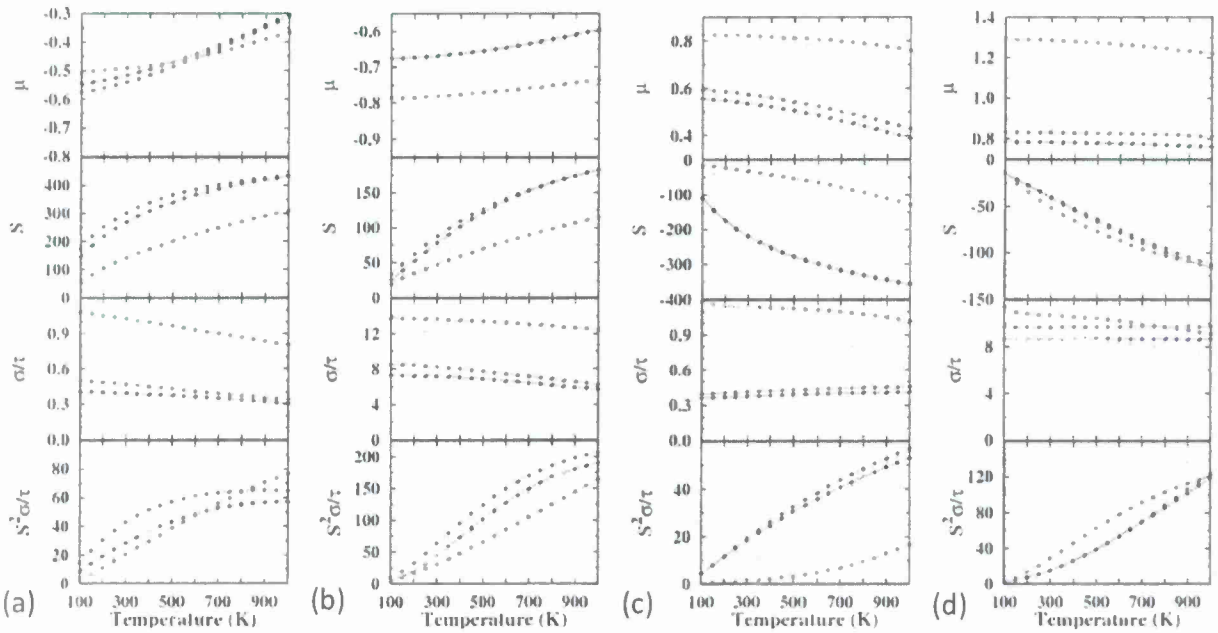

Figure 8. Transport properties for HfCoSb (○), ZrCoSb (◆), HfIrSb (■), and ZrIrSb (▼) as a function of temperature at the hole-concentration $nh=2\times10^{20}/cm^3$ (a), $nh=4\times10^{21}/cm^3$ (b), the electron-concentration $ne=2\times10^{20}/cm^3$ (c), and $ne=4\times10^{21}/cm^3$ (d). The units for μ, S, σ/τ, and $S^2\sigma/\tau$ are eV, μV/K, $10^{17}\Omega^{-1}cm^{-1}s^{-1}$, and 10^{14} μW $cm^{-1}K^{-2}s^{-1}$, respectively.

2. *Wiedemann-Franz law*

The HHs are considered to be promising thermoelectric materials because of their relatively large thermopowers and electrical conductivities. However, they show high thermal conductivities which limits their thermoelectric performance. The thermal conductivity is given by the sum of contributions from the electronic carriers (κ_{el}) and the lattice (κ_l). There are various attempts to reduce the thermal conductivity. The main approach is to reduce the lattice thermal conductivity. For this purpose, nanoparticle phonon scattering centers, points defects, and grain size reduction can be introduced in a bulk system. In experiments, to obtain the lattice thermal conductivity they measure the total thermal conductivity and then substract the electronic thermal conductivity which is usually calculated from Wiedeman-Franz (WF) law. Wiedemann-Franz law states that the ratio of the electronic contribution to the thermal conductivity and the electrical conductivity of a metal is proportional to the temperature, *i.e.* $\kappa_{el} / \sigma = \pi^2 / 3(k/e)^2 T = L_0 T$ where $L_0 = 2.45 \times 10^{-8}\ \mathrm{W\Omega K^{-2}}$ is obtained theoretically with electric field ***E***=0 and known as the Lorenz number. We note here that experimental measurements are conducted at electric current **J**=0, where the electronic thermal conductivity at constant electric current is given as $\kappa_{el,J} = \kappa_{el,E} + S^2 \sigma T$ We have calculated Lorenz number (L) at constant **E** and **J** using calculated electrical conductivity and electronic thermal conductivity, which is compared with. The ratio between L / L_0 is given as κ_E / κ_{WF} for constant **E** and κ_J / κ_{WF} for constant **J** in Fig. 9. It can be seen that (i) there is a large deviation between $\kappa_{el,E}$ or $\kappa_{el,J}$ and κ_{WF} at low *n* and high *T*. (ii) at high *T*, $\kappa_{el,E}$ is overestimated (~60% at 800 K) when WF law is used. As a result, κ_l is underestimated significantly. Thus, it needs caution to estimate the electronic thermal conductivity using the WF law.

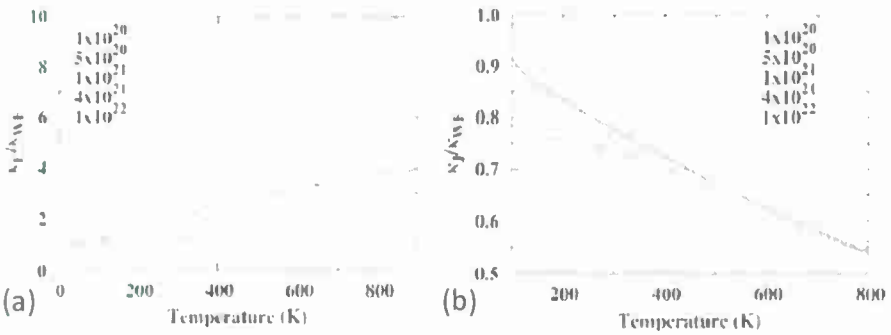

Figure 9. The ratio between the electronic thermal conductivity at constant E and with WF law (a), and at constant J and with WF law (b).

3. *Validity of rigid band approximation*

The transport properties of thermoelectric compounds can be calculated theoretically using the band structure and Boltzmann transport equations, where the rigid band approximation (RBA) is employed. According to the RBA, doping a system does not change its band structure but only the chemical potential. This approximation is widely used in theoretical calculations of transport properties of doped semiconductors and is a reasonably good approximation when the doping level is not very large. However, Sekimoto *et al.* observed that ZrCoSb gives high

power factor with 15 % of Sn doping in the compounds, which may affect its band structure. Therefore it is necessary to examine carefully the validity of the RBA in highly doped system. We have investigated the effect of impurity in the band structure of HfCoSb and hence their transport properties. As shown in the Fig. 10, a system doped with the same valent atom such as Zr (Fig.10 (b)) or Bi (Fig. 10(c)) does not change its band structure significantly compared with that of HfCoSb. In contrast, systems doped with different valent atom result in a drastic change of the band structure. We have also calculated the effect of changed band structure in their transport properties which is shown in Fig. 5. We observe a significant reduction of thermopower which may be caused from the removal of degeneracy in the band structure. Interestingly, the thermopower of $HfCoSb_{0.75}X_{0.25}$ with X=Ge, Sn, and Pb are nearly the same even though their band structures are slightly different.

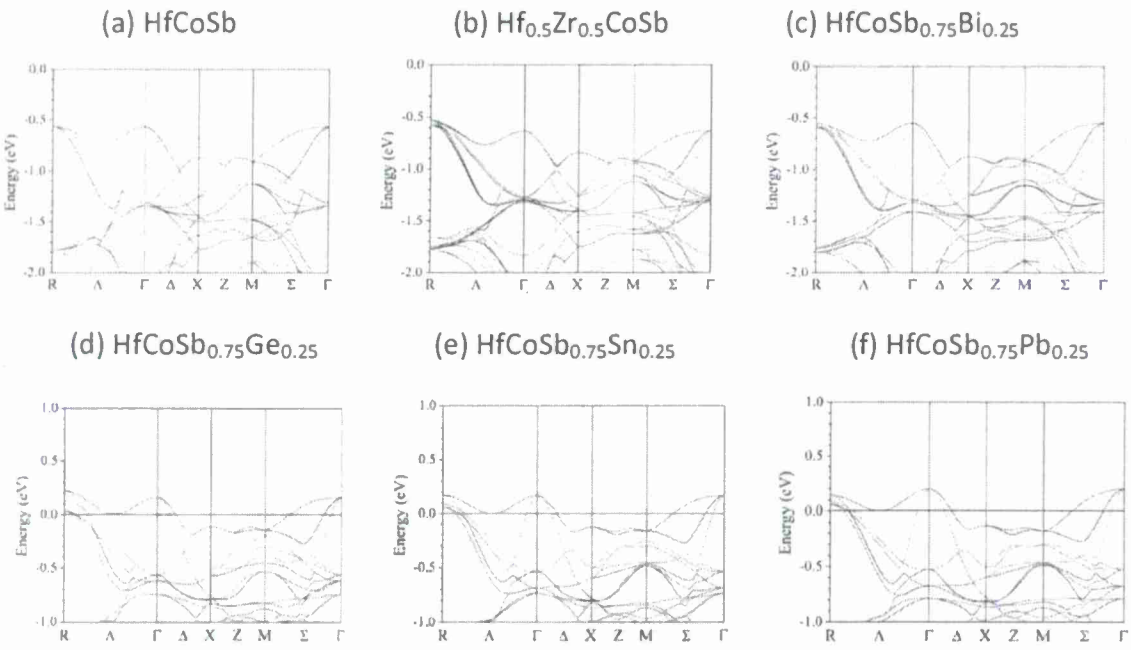

Figure 10. The band structure of impurity doped HfCoSb compounds.

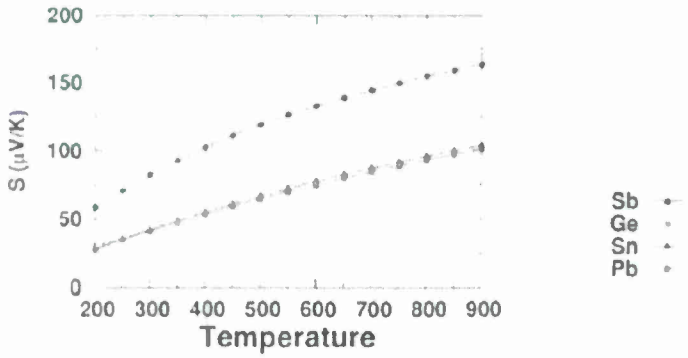

Figure 11. The thermopower of impurity-doped HfCoSb compounds.

4. ***Zr0.5Hf0.5IrxCo1-xSb with 0≤x≤1***

One way to reduce the thermal conductivity is introducing mass fluctuation phonon scattering. We have studied the effect of Co substitution with Ir in $Zr_{0.5}Hf_{0.5}CoSb$ on their band structure, which is shown in Fig. 12. In these calculations, we have included spin orbit interaction (SOI). It can be seen that the degeneracy removes and the position of the valence band maximum changes from R to Γ point when the content of Ir increases. This may affect their thermoelectric behavior significantly.

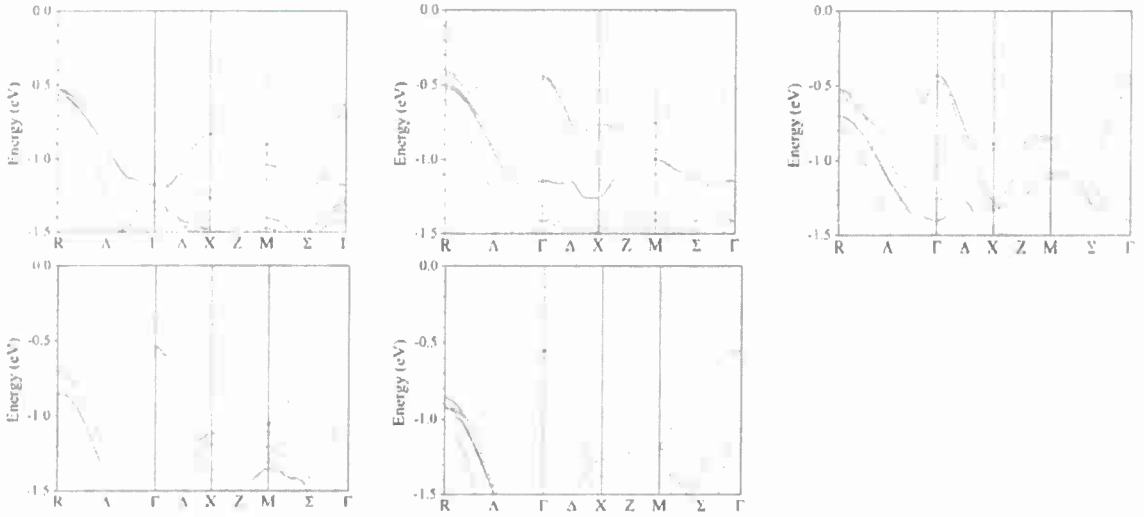

Figure 12. The band structure of Zr0.5Hf0.5Ir*x*Co*1-x*Sb with (a) x=0, (b) x=0.25, (c) x=0.5, (d) x=0.75, and (e) x=1.0.

C. Chemical Synthesis of Thermoelectric Nanoparticles

Our efforts have yielded well-studied routes towards facile, scalable synthesis of binary metallic nanoparticles for use in thermoelectric applications. These particles were produced both as nanoinclusions for the bismuth telluride based nanocomposites and as bulk, one-component nanostructured materials. Specifically, we have synthesized Ag_2Te, Bi_2Te_3, Sb_2Te_3, and Bi-Sb-Te phases. We have additionally fabricated single metal nanoparticles (e.g. Bi, Ag, Te, Ni, Bi-Sb) for use as nanoinclusion phases in bulk matrices as well as for nanoscale reagents in conversion reactions. Up to two gram batches of the thermoelectric nanoparticles were produced. Examples of the nanoparticles are shown in the transmission electron microscope images in Fig 13.

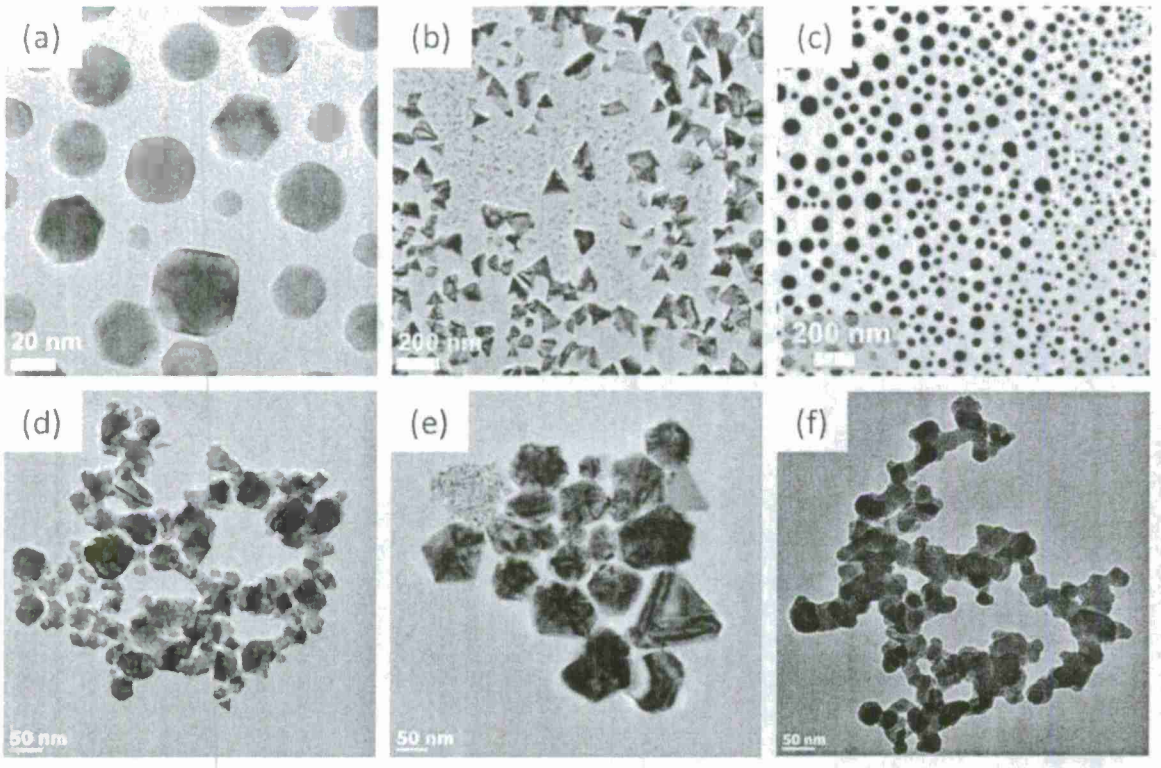

Figure 13. Nanoparticles synthesized by solution-phase, wet-chemical reactions used as nanoinclusions. (a) Bi, (b) Sb, (c) $Bi_{0.12}Sb_{0.88}$, (d) Ag_2Te, (e) Ag, and (f) Ni.

Silver Telluride (Ag_2Te)

A significant effort was devoted to the development of a *facile* and *scalable* method for the synthesis of nanoscale Ag_2Te nanoparticles. While we were able to produce single-phase, Ag_2Te particles in the range of 50-200 nm, further reduction in particle size was not achieved. We were able to reproducibly obtain nanometer-scale Ag_2Te particles in a two-step process through the reaction of $AgNO_3$ with preformed Te nanosheets and nanoscrolls.

Our method involves the reaction of silver nitrate ($AgNO_3$) and sodium metatellurate (Na_2TeO_4) in high-boiling tetraethylene glycol (TEG).Though initial successes were obtained by directly reacting Ag^+ and Te^{6+} cations in tetraethylene glycol, reaction pathway studies indicated this method first yielded elemental Ag particles, then elemental Te particles, and finally the final binary Ag_2Te phase. Rather than direct formation of the binary phase, as is observed with coprecipitation and coreduction methods for other bimetallic phases, time- and temperature-based aliquot studies suggest that the formation of Ag_2Te requires zero-valent Te in order to proceed. This is supported by the reaction of Ag^+ solutions with cationic solutions of Te at high temperatures, which yields predominantly Ag particles at temperature below that of the thermal decomposition point of the Te precursor. The synthesis of Ag_2Te proceeds by injecting $AgNO_3$ into preformed, PVP-stabilized Te particles, reproducibly yielding submicron scale particles of Ag_2Te. Powder XRD confirms the presence of Ag_2Te for samples obtained by heating solution of PVP and Na_2TeO_4 to 270 °C, allowing the Te particles to age for 1 h while

cooling to 180 °C, injecting a solution of $AgNO_3$, and finally allowing it to react at 180 °C for 1-2 h. The diffraction peaks are slightly broader than those observed through the direct addition of both Ag and Te (longer heating to obtain reaction completion, presumably leading to larger particle sizes of both Ag en route and then Ag_2Te). TEM images for Ag_2Te nanoparticles obtained through this route (Fig. 13) reveal particles sizes of under 50-100 nm. Trace amounts of sheetlike particles are still present, though imaging supports our hypothesis that the thin sheet and scroll-like Te particles are consumed in process of intermetallic formation.

Given the larger particles sizes of Ag_2Te samples (50-100 nm) and the broad distribution of both size and shape, efforts were made to lower the synthetic temperatures, ideally impeding particle growth by limiting the available energy. To this effect, we explored external reductants (i.e. sodium borohydride, $NaBH_4$) to nucleate the preformed Te particles, which we have previously shown necessary for the formation of the final Ag_2Te phase. Additionally, we investigated the effects of surfactant addition at various points during the reaction.

Reactions at varying temperatures and heating durations imply that Ag_2Te formation through the injection of $AgNO_3$ requires the presence of reduced Te in solution. After repeated synthetic attempts, it is apparent that the initial PVP/Te solution must reach at least 250 °C in order to yield crystalline Te and that an aging period of 45-60 min is necessary for reaction completion (yields large amounts of Ag otherwise). These lower synthetic temperatures lead to particle sizes and morphologies which is in the desirable size regime, as shown in Fig. 5. However, these are not fully converted presumably because there is not enough energy to convert fully to Ag_2Te. The particles below (Fig. 14) are a mixture of Te, Ag, and Ag_2Te.

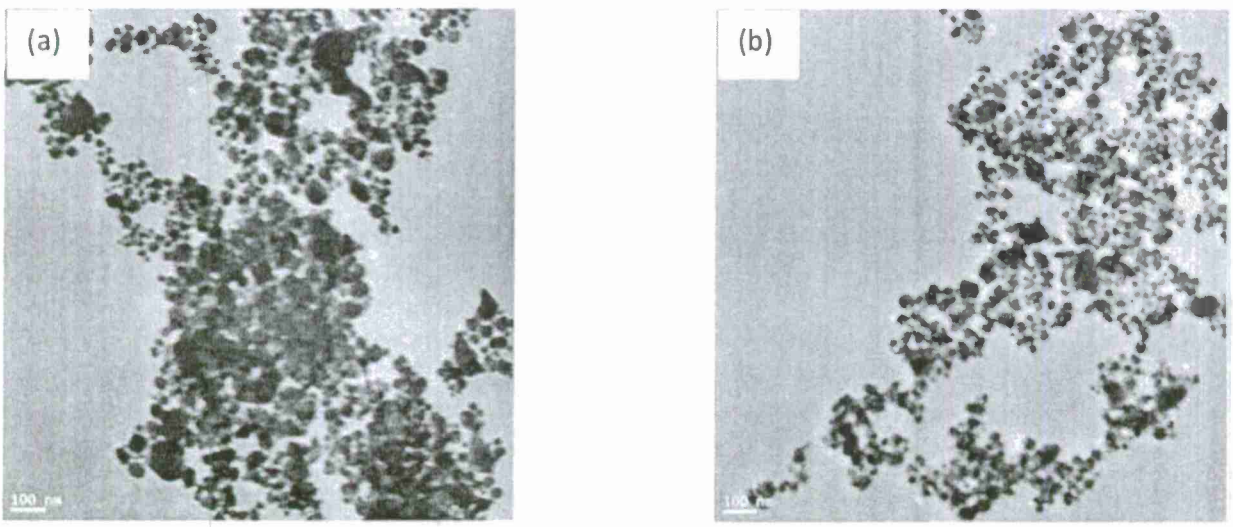

Figure 14. Ag_2Te, Ag and Te nanoparticles formed by lower temperature reaction.

Bismuth Telluride –Based Thermoelectric Nanoparticles

Nanoparticle thermoelectric materials were also produced and were consolidated for thermoelectric transport measurements. For nanoparticle material systems were chemically synthesized: **Bi_2Te_3**, **Sb_2Te_3**, **$Bi_{0.5}Sb_{1.5}Te_3$** and a **composite of Bi_2Te_3 in Sb_2Te_3** combined in the ratio of 2:3. Below is a summary of the procedures used for the chemical synthesis of these thermoelectric nanoparticles .

Bi_2Te_3 particles were obtained by injecting $BiCl_3$ into a freshly prepared Te nanoparticle solution. Na_2TeO_4 and PVP were dissolved in solution, heated to 260°C and allowed to anneal for 2-3 hours. $BiCl_3$ was dissolved in a separate volume of TEG and then injected over 15-20 min into the Te solution at 260°C. A freshly prepared solution of $NaBH_4$ was injected over 5 min after completely adding the Bi solution at 280°C. The solution was allowed to anneal for 4-5 hours at 260°C to obtain reaction completion and then cooled and washed.

Similar to the process mentioned above, **Sb_2Te_3** particles were obtained by injecting $SbCl_3$ into a freshly prepared Te nanoparticle solution. Na_2TeO_4 and PVP were dissolved in solution, heated to 270°C and allowed to annealed for 2-3 hours. $SbCl_3$ was dissolved in a separate volume of TEG and then injected over ~30 min into the Te solution at 270°C. A freshly prepared solution of $NaBH_4$ was injected over 10 min after completely adding the Sb solution at 240°C. The solution was allowed to anneal at 260°C for 4-5 hours to obtain reaction completion and then cooled and washed.

Mixed phase Bi-Sb-Te particles were obtained by injecting a mixed cation solution of Bi and Sb into preformed Te nanoparticles. Na_2TeO_4 and PVP were dissolved in solution, heated to 270°C and allowed to annealed for 2-3 hours. $SbCl_3$ and $BiCl_3$ were dissolved in a separate volume of TEG and then injected over ~20 min into the Te solution at 280°C. A freshly prepared solution of $NaBH_4$ was injected over 10 min after completely adding the Sb/Bi solution at 270°C. The solution was allowed to anneal at 280°C for 3-4 hours to obtain reaction completion and then cooled and washed.

XRD studies confirm literature reports (e.g. Schaak et al. J. Mater. Chem. 2010) of inhomogeneous alloying. The composition of the resulting powder is a mixture of both Sb_2Te_3 and various compositions of the $(Bi_{1-x}Sb_x)_2Te_3$ solid solution. According to literature precedents, this can be converted with annealing at 500°C to a single composition, suggesting that consolidation through hot pressing would yield a dense pellet of a single composition.

The particles obtained for these phases typically adopt morphologies of hexagonal nanoplatelets, 20-50 nm in thickness and up to 200 nm in diameter. Time and temperature resolved studies suggest that elemental Te is required for conversion to the binary phase. Additionally, the alloying seems to occur as a diffusion-based reaction between bismuth telluride and antimony telluride. Bi_2Te_3 requires a higher reaction temperature (> 250-260°C) than Sb_2Te_3 (> 220-230°C), so alloying reactions will yield only Sb_2Te_3 if the temperature is not

sufficiently high. Finally, the plate-like binary nanoparticles seem to grow perpendicular to the growth direction of the Te nanowires, which is consistent with literature reports.

D. $Zr_{0.25}Hf_{0.75}Sn_{0.975}Sb_{0.025}$/Co@$SiO_2$ nanocomposites

$Zr_{0.25}Hf_{0.75}Sn_{0.975}Sb_{0.025}$/Co@$SiO_2$ nanocomposites were prepared by mixing different weight percentage of Co@SiO_2 core@shell nanoparticles with $Zr_{0.25}Hf_{0.75}Sn_{0.975}Sb_{0.025}$ matrix material. The samples were consolidated using hot press at 850 °C. The thermal and electrical transport properties are also reported.

Introduction of binary nanoscale metallic@insulator/semiconductor core@shell in half-Heusler matrix may be prove to beneficial by increasing electrical conductivity due to the presence of metallic core and at the same time decreasing thermal conductivity by phonon scattering at the nanoparticles boundaries. Surfactant free Co nanoparticles were synthesized by sodium borohydride reduction in aqueous solution and coated with 2 nm SiO_2 shell. Co@SiO_2 core@shell (20@2 nm) nanoparticles were thoroughly mixed with half-Heusler $Zr_{0.25}Hf_{0.75}NiSn_{0.975}Sb_{0.025}$ matrix in different weight percentage. The samples were compacted using hot press at 850 °C and transport properties were measured on compacted samples. Figure 15 shows the temperature dependence thermal conductivity of $Zr_{0.25}Hf_{0.75}NiSn_{0.975}Sb_{0.025}$/Co@$SiO_2$ nanocomposites. It is clear from figure 1A that total thermal conductivity of matrix materials decreased by introduction of 1 and 2 weight percentage of Co@SiO_2 nanoparticles. Further analyzing the thermal conductivity (Figure 15 B & C), it was found that the deceased in thermal conductivity is mainly due to electronic contribution. We are in process of analyzing the microstructure of the samples, however, it is speculated that 2 nm SiO_2 shell may not be enough to protect Co from diffusing into the matrix materials during compaction at 850 °C.

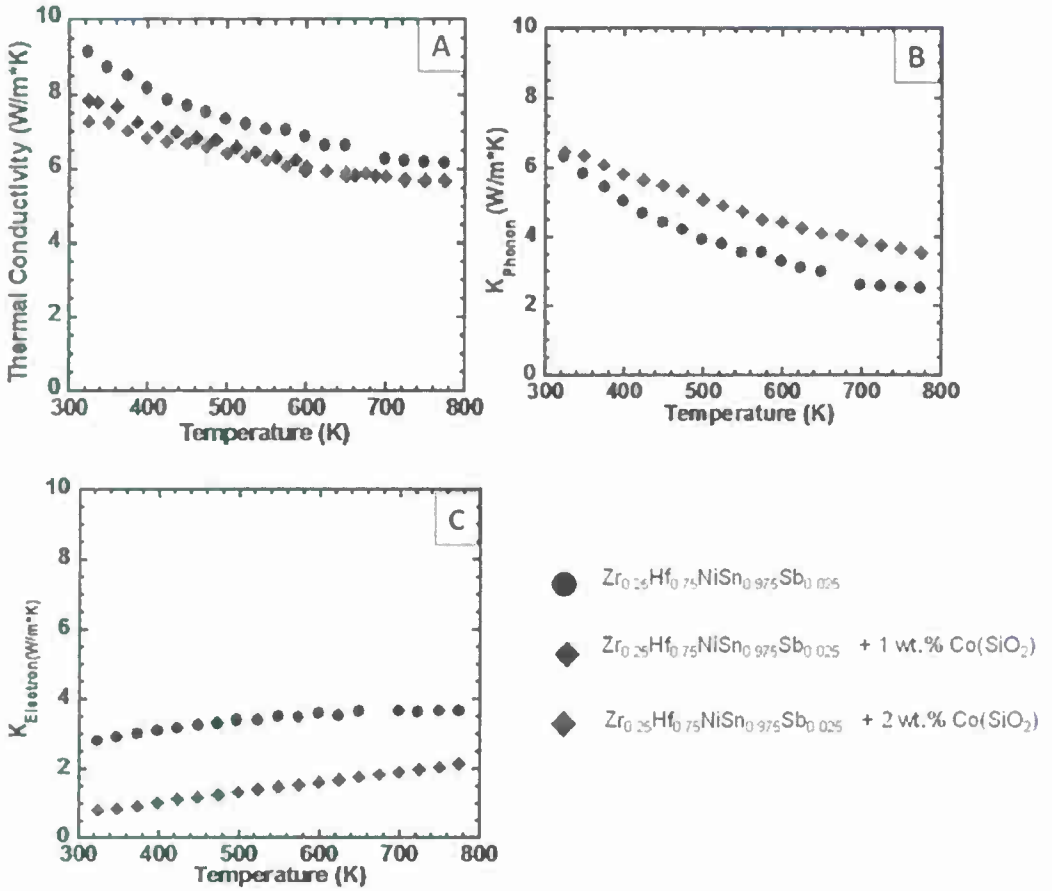

Figure 15. Temperature dependence thermal conductivity of samples (A) total thermal conductivity (B) lattice thermal conductivity (C) electronic contribution of thermal conductivity.

Figure 16 shows the temperature dependence electrical conductivity and Seebeck coefficient of $Zr_{0.25}Hf_{0.75}NiSn_{0.975}Sb_{0.025}/Co@SiO_2$ nanocomposite. Figure 2A show that electrical conductivity of the matrix materials is decreased by introduction of 2 wt % $Co@SiO_2$ nanoparticles. It is not clear what caused the decrease in electrical conductivity of the nanocomposite, however, it might be possible that the ferromagnetic Co nanoparticles may have created a local magnetic field. This local magnetic field might have caused some scattering of electrons, which then resulted in decrease in electrical conductivity. Figure 16B shows that the Seebeck coefficient of the nanocomposite sample decreases compared to matrix material.

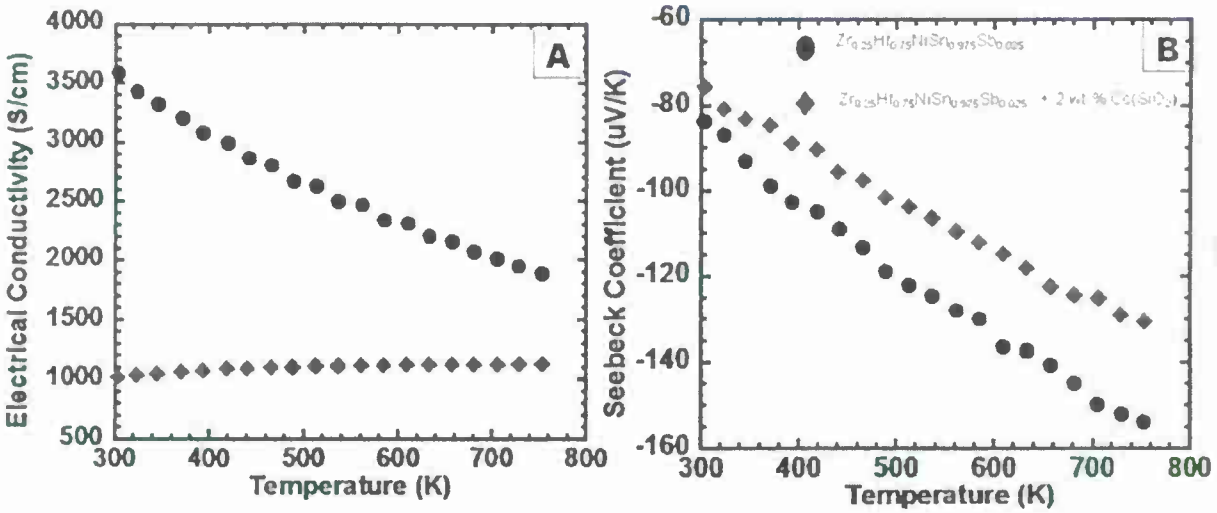

Figure 16. Temperature dependence (A) electrical conductivity and (B) Seebeck coefficient of $Zr_{0.25}Hf_{0.75}NiSn_{0.975}Sb_{0.025}$ /2 wt % Co@SiO_2 nanocomposites. Figure legends are shown figure 16B for both figures.

Figure 17 shows temperature dependence ZT of nanocomposite sample and compared with matrix material. It was found that ZT of the nanocomposite has decreased compared to matrix material over the same temperature range.

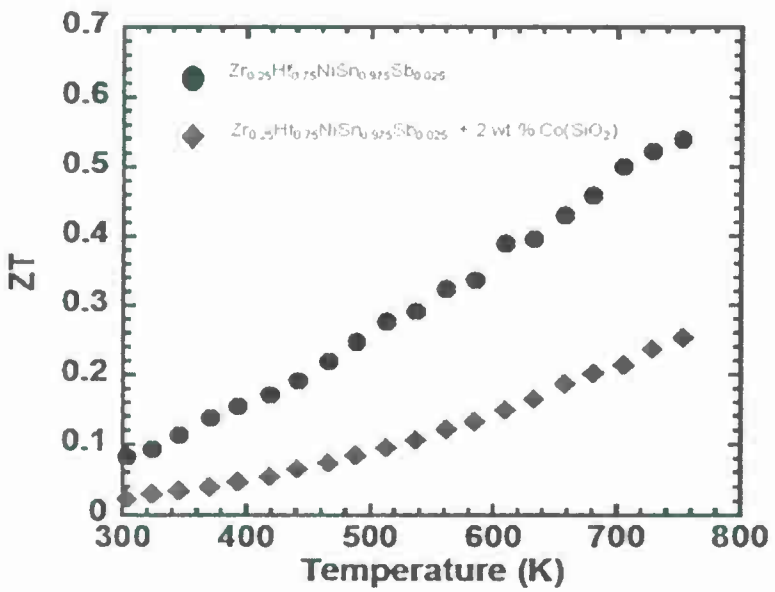

Figure 17. Temperature dependence ZT of matrix material and nanocomposite containing 2 wt% Co@SiO_2 nanoparticles

E. Mechanical Testing

Measurements were made of the Young's modulus and toughness of half-Heusler bulk materials with compositions $[Zr_{0.5}Hf_{0.5}][Ni_{1-y}Pd_y][Sn_{0.99}Sb_{0.01}]$ and $[Zr_{0.5}Hf_{0.5}][Co_{1-}$

$_y$Ir$_y$][Sb$_{0.99}$Sn$_{0.01}$]. The mechanical integrity of promising thermoelectric material is critical for practical energy conversion applications. In addition to the thermal gradient imposed under steady-state conditions, the TE materials must survive thousands of heating and cooling cycles if they are to be useful for long term applications. Measurements of physical and mechanical properties were used to develop an understanding of the relationship of the structure and processing methods to the performance of the materials. Synthesis and processing will be optimized to meet the needs of engineered devices.

A microhardness tester will be used to obtain hardness measurements and determine the modulus of elasticity for thermoelectric samples. These tests will be used to assess homogeneity of mechanical properties as a function of processing parameters. Properties will be measured in conjunction with thermal fatigue testing to assess life-cycle performance. Static tensile and fatigue loading will be performed on larger samples (~1 inch in length) as needed to study the mechanical and fracture behavior of these materials utilizing a 1000 lb Fullam tensile substage compatible with in-situ electron microscopy (available at UNO). This data will aid in optimizing process parameters and validating homogeneity in properties for use in thermoelectric devices.

A total of 5 *n*-type $Zr_{0.25}Hf_{0.75}NiSn$ half-Heusler nanocomposite samples with excess Ni added (% Ni = 0, 0.5, 1, 1.5 and 5) were tested by microindentation. (The addition of the excess Ni can produce a half-Heusler/full-Heusler nanocomposite.) Vickers hardness data were obtained for indentation loadings of 100gf and 200gf, respectively. The base composition has a reported hardness of 874 HV0.2. $Zr_{0.25}Hf_{0.75}NiSn$ series with Ni inclusions demonstrated a range of 884 HV0.2 to 1045 HV0.2. These hardness values are in the high end of the range of hardness values for the half-Heusler compounds previously reported. However, whereas the modulus values of the compositions with nanoinclusions were all within 5% of the bulk half-Heusler of nominal composition, the hardness of the compositions with nanoinclusions varied by up to 20% when compared to that of the bulk half-Heusler of nominal composition.

Evaluation of the fracture toughness of half-Heusler compounds formed using different synthesis methods was performed. Three sets of samples of the composition $Ti_{0.5}Hf_{0.5}Co_{0.5}Ir_{0.5}Sb_{1-x}Sn_x$ at x= 0, 0.1, 0.2, 0.3, and 0.4. Each set was formed using a different method as follows: (1) high-energy ball-milling for 10hr and hot pressed at 950°C and 100MPa; (2) high temperature solid state reaction at 900°C for 30 days and hot pressed at 950°C; and 100MPa, and (3) high temperature solid state reaction at 900°C for 30 days then high-energy ball-milling for 10hr and hot pressed at 950°C and 100MPa. Fracture toughness testing was performed by using microindentation along with optical microscopy to determine the lengths of the cracks emanating from the corners of the indentations. Samples of similar composition produced using methods (1) and (3), which include the ball-milling step, possessed similar fracture toughness values (to within a standard deviation). Ball-milled samples prepared by method (1) produced fracture toughness results between 2.2 MPa $m^{½}$ and 2.6 MPa $m^{½}$ with standard deviations between 0.1 MPa $m^{½}$ and 0.4 MPa $m^{½}$. No trend is observed with compositional changes. Similar results were obtained from samples prepared by method (3) with fracture toughness values ranging from 2.5 MPa $m^{½}$ and 3.0 MPa $m^{½}$ and standard

deviations between 0.2 MPa $m^{1/2}$ and 0.3 MPa $m^{1/2}$. The samples prepared by method (2), with no ball-milling step, had slightly higher fracture toughness values of 2.7 MPa $m^{1/2}$ to 4.1 MPa $m^{1/2}$ and higher standard deviation (between 0.3 and 0.7). For these samples, the compositions of increasing tin content possessed the lower fracture toughness. The fracture toughness results are in line with the fracture toughness values obtained for other bulk half-Heusler compounds previously reported.

Hardness testing of 6 $Zr_{0.25}Hf_{0.75}Ni_{1+x}Sn0_{.975}Bi_{0.025}$ (x=0.0, 0.02, 0.03, 0.04, 0.06, and 0.10) samples is currently ongoing. Hardness loadings of 200gf have been determined to be the optimum loadings for this set of samples. The hardness value of the base composition is 561HV0.2; for compositions with x values of 0.02, 0.03, and 0.04, the hardness values are similar and range from 802HV0.2 to 834HV0.2. Note that the hardness increases significantly from the base composition with the additional nickel content.

V. WORK PRODUCTS

A. Journal Articles and Refereed Conference Proceedings

[1] M.-S. Lee, F. P. Poudeu, and S. D. Mahanti, "Electronic structure and thermoelectric properties of Sb-based semiconducting half-Heusler compounds," *Phys. Rev. B* 83, p. 085204, 2011. http://dx.doi.org/10.1103/PhysRevB.83.085204 IF: 3.772

[2] P. Maji, N. J. Takas, D. K. Misra, H. Gabrisch, K. L. Stokes, and P. F. P. Poudeu, "Effects of Rh on the thermoelectric performance of the p-type $Zr_{0.5}Hf_{0.5}Co_{1-x}Rh_xSb_{0.99}Sn_{0.01}$ half-Heusler alloys," *J. Solid State Chem.* 183, pp. 1120-1126, 2010. http://dx.doi.org/10.1016/j.jssc.2010.03.023 IF: 2.261

[3] J. P. A. Makongo, D. K. Misra, J. Salvador, N. J. Takas, G. Wang, M. R. Shabetai, A. Pant, P. Paudel, C. Uher, K. L. Stokes, and P. F. P. Poudeu, "Thermal and Electronic Charge Transport in Bulk Nanostructured $Zr_{0.25}Hf_{0.75}NiSn$ Composites with Full-Heusler Inclusions," *J. Solid State Chem.* 84, pp. 2948-2960, 2010. http://dx.doi.org/10.1016/j.jssc.2011.08.036 IF: 2.261

[4] N. Takas, P. Sahoo, D. Misra, H. Zhao, N. Henderson, K. L. Stokes, and P. Poudeu, "Effects of Ir Substitution and Processing Conditions on Thermoelectric Performance of $Zr_{0.5}Hf_{0.5}Co_{1-x}Ir_xSb_{0.99}Sn_{0.01}$ Half-Heusler Alloys," *J. Electron. Mater.* pp. 1-8, 2011. http://dx.doi.org/10.1007/s11664-010-1501-0 IF: 1.39

[5] J. Yao, N. J. Takas, M. L. Schliefert, D. S. Paprocki, P. E. R. Blanchard, H. Gou, A. Mar, C. L. Exstrom, S. A. Darveau, P. F. P. Poudeu, and J. A. Aitken, "Thermoelectric properties of p-type $CuInSe_2$ chalcopyrites enhanced by introduction of manganese," *Phys. Rev. B* 84, p. 075203, 2011. http://dx.doi.org/10.1103/PhysRevB.84.075203 IF: 3.772

[6] P. Sahoo, D. K. Misra, G. S. Chaubey, J. Salvador, N. Takas, and P. F. P. Poudeu, "Thermal conductivity of nickel oxide nanoparticles synthesized by combustion method," in *Functional Oxide Nanostructures and Heterostructures, Mater. Res. Soc. Symp. Proc.* vol. 1256, Warrendale, PA: Materials Research Society, 2010, pp. 1256-N06-21. http://dx.doi.org/10.1557/proc-1256-n06-21

[7] R. Yaqub, P. Sahoo, J. P. A. Makongo, W. M. Nolting, N. Takas, P. F. P. Poudeu, and K. L. Stokes, "The Role NiO of Nanoinclusions on High Performance Half Heusler

Thermoelectric Materials," in *Thermaelectric Materials—Growth, Properties, Novel Characterization Methods, and Applications, Mater. Res. Soc. Symp. Proc.* vol. 1267E, J. D. Baniecki, Ed. Warrendale, PA: MRS, 2010, pp. 1267-DD05-18. http://dx.doi.org/10.1557/PROC-1267-DD05-18

[8] G. S. Chaubey, Y. Yao, J. P. A. Makongo, P. Sahoo, P. F. P. Poudeu, and J. B. Wiley, "Synthesis and thermal stability of HfO_2 nanoparticles," in *Functional Oxide Nanastructures and Heterostructures, Mater. Res. Sac. Symp. Proc.* vol. 1256E, Warrendale, PA: Materials Research Society, 2010, article# 1256-N16-35. http://dx.doi.org/10.1557/proc-1256-n16-35

[9] J. D. Germond, P. J. Schilling, N. J. Takas, and P. F. P. Poudeu, "Thermoelectric performance of nanostructured ZrNiSn compounds synthesized by mechanical alloying," in *Thermoelectric Materials—Growth, Properties, Novel Characterization Methods, and Applicatians, Mater. Res. Soc. Symp. Proc.* vol. 1267E, Warrendale, PA: Materials Research Society, 2010, article# 1267-DD03-12. http://dx.doi.org/10.1557/proc-1267-dd03-12

[10] J. P. A. Makongo, D. K. Misra, J. Salvador, N. J. Takas, K. L. Stokes, H. Gabrisch, and P. F. P. Poudeu, "Effect of partial filling of the structural vacant sites on the thermoelectric properties of $Zr_{0.25}Hf_{0.75}NiSn$ half-Heusler alloy," in *Thermaelectric Materials—Growth, Praperties, Navel Characterization Methods, and Applicatians, Mater. Res. Soc. Symp. Prac.* vol. 1267E, J. D. Baniecki, Ed. Warrendale, PA: MRS, 2010, article# 1267-DD05-11/1-6. http://dx.doi.org/10.1557/PROC-1267-DD05-12

[11] J. P. A. Makongo, P. Paudel, D. K. Misra, and P. F. P. Poudeu, "Thermoelectric Properties of $Zr_{0.5}Hf_{0.5}Ni_{0.8}Pd_{0.2}Sn_{0.99}Sb_{0.01}$ half-Heusler Alloy with WO_3 Inclusions," in *Thermoelectric Materials—Growth, Properties, Novel Characterization Methods, and Applications, Mater. Res. Sac. Symp. Proc.* vol. 1267E, J. D. Baniecki, Ed. Warrendale, PA: MRS, 2010, article# 1267-DD07-10. http://dx.doi.org/10.1557/PROC-1267-DD07-10

[12] D. K. Misra, J. P. A. Makongo, M. R. Shabetai, G. S. Chaubey, J. B. Wiley, K. L. Stokes, and P. F. P. Poudeu, "Structure and thermoelectric properties correlation in half-Heusler ZrNiSn-based bulk nano-composite materials by transmission electron microscopy," in *Thermaelectric Materials—Grawth, Praperties, Navel Characterization Methods, and Applications, Mater. Res. Soc. Symp. Proc.* vol. 1267E, Warrendale, PA: Materials Research Society, 2010, article# 1267-DD06-12. http://dx.doi.org/10.1557/proc-1267-dd06-12

[13] S. Sumithra, N. J. Takas, N. L. Henderson, W. M. Nolting, D. M. Misra, P. F. P. Poudeu, and K. L. Stokes, "Metal Nanoinclusions (Bi and Ag) in Bi_2Te_3 for Enhanced Thermoelectric Applications," in *Thermoelectric Materials—Growth, Properties, Novel Characterization Methods, and Applications, Mater. Res. Soc. Symp. Proc.* vol. 1267E, J. D. Baniecki, Ed. Warrendale, PA: MRS, 2010, article# 1267-DD07-11. http://dx.doi.org/10.1557/PROC-1267-DD07-11

[14] N. J. Takas, D. K. Misra, H. Gabrisch, and P. F. P. Poudeu, "Spinodal decomposition in off-stoichiometric $Zr_{0.5}Hf_{0.5}Co_{1-y}Ir_ySb_{1-z}Sn_z$ half-Heusler phases," in *Thermoelectric Materials—Grawth, Praperties, Novel Characterizatian Methads, and Applications, Mater. Res. Soc. Symp. Proc.* vol. 1267E, Warrendale, PA: Materials Research Society, 2010, article# 1267-DD07-07. http://dx.doi.org/10.1557/proc-1267-dd07-07

[15] M. A. Verges, P. J. Schilling, J. D. Germond, P. Upadhyay, W. K. Miller, N. J. Takas, and P. F. P. Poudeu, "Indentation Testing of Bulk $Zr_{0.5}Hf_{0.5}Co_{1-x}Ir_xSb_{0.99}Sn_{0.01}$ Half-Heusler Alloys," in *Thermoelectric Materials—Growth, Properties, Novel Characterization Methods, and Applications, Mater. Res. Soc. Symp. Proc.* vol. 1267E, Warrendale, PA: Materials Research Society, 2010, article# 1267-DD05-23. http://dx.doi.org/10.1557/PROC-1267-DD05-23

[16] M. A. Verges, P. J. Schilling, J. D. Germond, P. Upadyhay, W. K. Miller, P. Maji, N. J. Takas, and P. F. P. Poudeu, "Young's Modulus and Hardness of $Zr_{0.5}Hf_{0.5}Ni_xPd_{1-x}Sn_{0.99}Sb_{0.01}$ Half-Heusler Compounds," *Proceedings of the ASME 2010 International Mechanical Engineering Congress & Exposition* IMECE2010, p. 38988, 2010.

[17] J. Yao, N. J. Takas, M. L. Schliefert, D. S. Paprocki, P. E. R. Blanchard, H. Gou, A. Mar, C. L. Exstrom, S. A. Darveau, P. F. P. Poudeu, and J. A. Aitken, "Thermoelectric properties of p-type CuInSe_{2} chalcopyrites enhanced by introduction of manganese," *Physical Review B* 84, p. 075203, 2011. http://dx.doi.org/10.1103/PhysRevB.84.075203

B. Selected Presentations

[1] G. S. Chaubey, J. P. A. Makongo, Y. Yao, D. K. Misra, P. F. P. Poudeu, and J. B. Wiley, "Enhanced Thermoelectric Properties of In-situ Synthesized Half-Heusler/ HfO_2 Nanocomposites," presented at the *Materials Research Society Fall Meeting, Symposium LL: Thermoelectric Materials for Solid-State Power Generation and Refrigeration*, Boston, MA, 2010.

[2] P. Maji, J. P. A. Makongo, and P. F. P. Poudeu, "Thermoelectric Performance of the p-type $Zr_{0.5}Hf_{0.5}Co_{0.4}Rh_{0.6}Sb_{1-x}Sn_x$ ($0 \leq x \leq 0.5$) Half-Heusler Alloys," presented at the *Materials Research Society Fall Meeting, Symposium LL: Thermoelectric Materials for Solid-State Power Generation and Refrigeration*, Boston, MA, 2010.

[3] J. P. A. Makongo, J. Salvador, D. K. Misra, and P. F. P. Poudeu, "Simultaneous Reduction in Thermal Conductivity and Enhancement of Power Factor in High Performance n-type $Zr_{0.25}Hf_{0.75}Ni_{1+x}Sn$ ($0 \leq x \leq 0.1$) Half-Heusler Alloys," presented at the *Materials Research Society Fall Meeting, Symposium LL: Thermoelectric Materials for Solid-State Power Generation and Refrigeration*, Boston, MA, 2010.

AMRI
ADVANCED MATERIALS RESEARCH INSTITUTE

UNIVERSITY OF NEW ORLEANS

October 16, 2012

DARPA/DSO
Attn: Dr. Brian Holloway
DARPA Program Officer
3701 North Fairfax Drive
Arlington, VA 22203-1714

Re: DARPA Grant No. HR0011-08-1-0084, "Nanostructured Composite Materials for High Temperature Thermoelectric Energy Conversion," Final Technical Report, August 29, 2012

Dear Dr. Holloway:

Enclosed per the requirements of the above referenced Grant is one copy of our Final Technical Report dated August 29, 2012. Should you have any questions, please let me know.

Sincerely yours,

C. J. O'Connor

Charles J. O'Connor, Ph.D.
Principal Investigator and
Director of AMRI

CJOC/ird

cc: Dr. Alexander Ehrlich, GOR, Naval Research Laboratory (2 copies)
Mr. Michael Mutty, Grants Officer, DARPA/DSO (1 copy)
Ms. Marlo Ettien, AGO, ONR-Atlanta (2 copies)
DARPA Technical Information Library (1 copy)
Defense Technical Information Center (2 copies)

2048 Science Building *Lakefront Campus* 2000 Lakeshore Drive New Orleans, Louisiana 70148
504.280.6840 *fax* 504.280.3185 *e-mail* amri@uno.edu